Role of Al additions in wear control of nanocrystalline $Mo(Si_{1-x}Al_x)_2$ coatings prepared by double cathode glow discharge technique

J. Xu*[1], H. S. Fan[1] and Z. Y. Li[2]

Four kinds of nanocrystalline $Mo(Si_{1-x}Al_x)_2$ coatings with differing Al contents are prepared onto a Ti–6Al–4V substrates by a double cathode glow discharge apparatus. The microstructural features of the deposited coatings were characterised by X-ray diffraction, scanning electron microscopy and transmission electron microscopy. These coatings are composed of the equiaxed C40–$MoSi_2$ grains with the average grain size of ~5 nm. Nano-indentation measurements indicated that the hardness H, elastic modulus E and the H/E or H^3/E^2 ratio of the nanocrystalline $Mo(Si_{1-x}Al_x)_2$ coatings slightly increase with the increase in Al content. The tribological behaviour of the nanocrystalline $Mo(Si_{1-x}Al_x)_2$ coating sliding against a ZrO_2 ceramic ball at room temperature has been compared using a ball-on-disc type tribometer under unlubricated conditions. Experimental results showed that the specific wear rates of the nanocrystalline $Mo(Si_{1-x}Al_x)_2$ coatings decrease with increasing Al content and are dramatically reduced by more than 1–2 orders of magnitude over the uncoated Ti–6A1–4V. The enhancement of wear resistance of the nanocrystalline $Mo(Si_{1-x}Al_x)_2$ coatings by Al additions is correlated with the increased mechanical properties and the forming oxide layer by tribochemical reactions.

Keywords: Molybdenum silicides, Nanostructured materials, Friction/wear, Thin films

Introduction

Owing to their unique combination of high specific strength, excellent chemical stability and good biocompatibility, titanium alloys have found a wide range of applications ranging from aerospace and food processing to biomedical areas. Nevertheless, the poor tribological properties caused by relatively low surface hardness and high friction coefficient have seriously hindered extensive applications of titanium alloys in many sliding components, especially where high wear resistance is required.[1–3] One of the most promising ways to combat this problem is the application of different hard surface modified coatings on titanium alloys.[4,5] From a tribological perspective, molybdenum silicide ($MoSi_2$) can potentially be regarded as an attractive wear resistant and antifriction surface coating material suitable for extremely harsh working conditions because of its inherent high hardness and high elastic modulus.[6] For instance, Hawk and Alman[7] have compared the abrasive wear behaviour of monolithic $MoSi_2$ with refractory metals, aluminide and oxide ceramics. They found that the wear resistance of $MoSi_2$ is comparable to that of oxide ceramics and markedly superior to that of refractory metals and aluminide. A major challenge in the wide application of $MoSi_2$, like many other intermetallic compounds, is to overcome its intrinsic brittleness at ambient temperature. In general, wear resistance of brittle materials is dependent on mechanical properties and microstructural features, and thus, the improved mechanical properties, such as hardness and fracture toughness, and microstructural refinement are beneficial for the enhanced wear resistance.[8,9] Different from ionic or covalent bonding seen in ceramics, the partial metallic character of bonding in $MoSi_2$ provides the possibility of alloying as a potential avenue to reduce the low temperature brittleness. $MoSi_2$ is a dimorph compound, which possesses a hexagonal close packed C40 structure with $P6_222$ space group between the melting point and 1900°C and a tetragonal body centred $C11_b$ structure with I4/mmm space group below this temperature.[10,11] The theoretical and experimental work suggested that alloying $C11_b$ $MoSi_2$ with different elements, such as Al, Mg, Ti, V, Nb and Re, has appreciable effect on its mechanical properties.[12–14] Among possible substitutional

[1]Department of Material Science and Engineering, Nanjing University of Aeronautics and Astronautics, 29 Yudao Street, Nanjing 210016, China
[2]Institute of Mechanics, Chinese Academy of Sciences, Beijing 100190, China

*Corresponding author, email xj_msc@nuaa.edu.cn

Published by Maney on behalf of the Institute
Received 11 November 2012; accepted 25 January 2013
DOI 10.1179/1743284713Y.0000000218

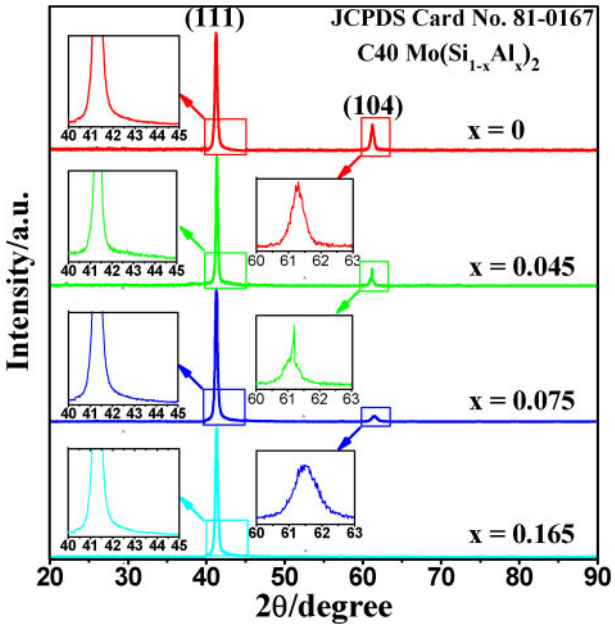

1 XRD patterns of the $Mo(Si_{1-x}Al_x)_2$ nanocrystalline coatings

alloying elements, Al seems to be the most effective in improving the ductility and oxidation resistance of monolithic $MoSi_2$, since Al enhances the metallic character of bonding in $MoSi_2$ and has strong affinity to oxygen.[15,16] In comparison with the well investigated $C11_b$ structured $MoSi_2$, little work is addressed upon the issue of the mechanical behaviour of C40 structured $MoSi_2$, which is mainly attributed to the difficulty in fabricating the metastable C40 structured $MoSi_2$ with conventional processing. Theoretical calculations have revealed that the reduction in symmetries from $C11_b$ structured to C40 structured $MoSi_2$ can lead to an improvement in ductility.[17]

In the present work, to improve the tribological behaviour of Ti–6A1–4V alloy, four kinds of sputter deposited nanostructured C40 $Mo(Si_{1-x}Al_x)_2$ coatings have been prepared on Ti–6A1–4V alloy substrates by a double cathode glow discharge technique. Their microstructure was characterised by X-ray diffraction (XRD), scanning electron microscopy (SEM) and transmission electron microscopy (TEM). The influence of Al additions on the hardness H, elastic modulus E and wear resistance of the resultant coatings of nanostructured C40–$Mo(Si_{1-x}Al_x)_2$ coatings was explored. To gain a deeper insight into wear mechanisms, the morphologies and phase composition of worn surfaces were analysed using SEM and X-ray photoelectron spectroscopy (XPS).

Experimental

The nanocrystalline $Mo(Si_{1-x}Al_x)_2$ coatings were deposited onto Ti–6A1–4V alloy substrates by a double cathode glow discharge apparatus, as described elsewhere.[18] Inside the chamber, one cathode is used as the target, and the other is used as the substrate. The glow discharge sputtering conditions were as follows: base pressure, 4×10^{-4} Pa; target electrode bias voltage, −900 V; substrate bias voltage, −300 V; substrate temperature, 850°C; working pressure, 35 Pa; parallel distance between the source electrode and the substrate, 12 mm; and treatment time of 3 h. The sputter targets were fabricated by employing cold compacting technology under a pressure of 600 MPa from ball milled Mo (99·99% purity), Al (99·99% purity) and Si powders (99·99% purity). The substrate material was Ti–6Al–4V in the form of discs with a diameter of 40 mm and a thickness

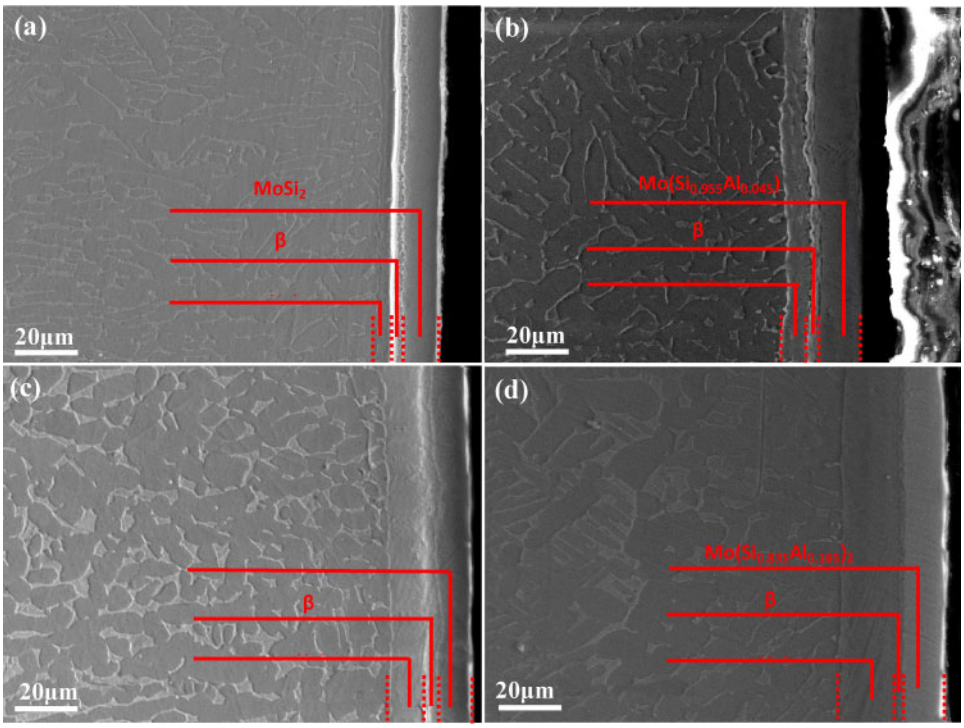

2 SEM cross-section micrograph of the as-deposited $Mo(Si_{1-x}Al_x)_2$ coatings (a) $MoSi_2$ coating; (b) $Mo(Si_{0.955}Al_{0.045})_2$ coating; (c) $Mo(Si_{0.925}Al_{0.075})_2$ coating; (d) $Mo(Si_{0.835}Al_{0.165})_2$ coating

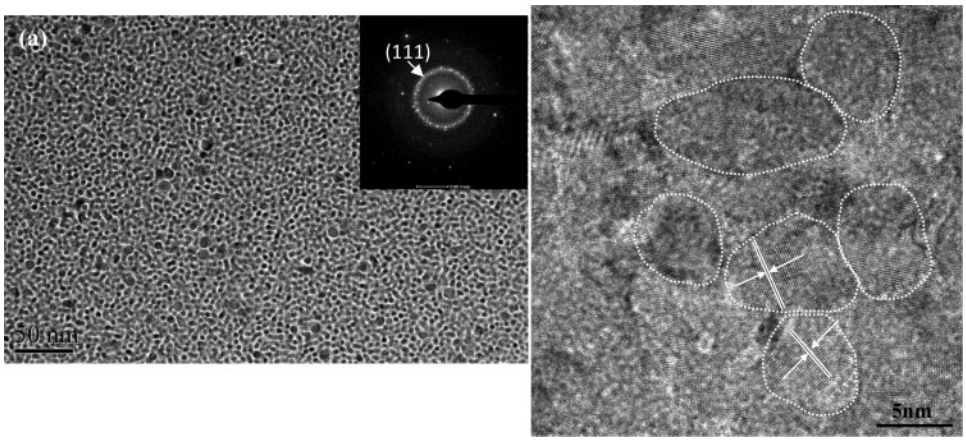

3 (a) A plan-view TEM bright-field image of the as-deposited $Mo(Si_{0.955}Al_{0.045})_2$ coating; (b) HRTEM image of as-deposited $Mo(Si_{0.955}Al_{0.045})_2$ coating

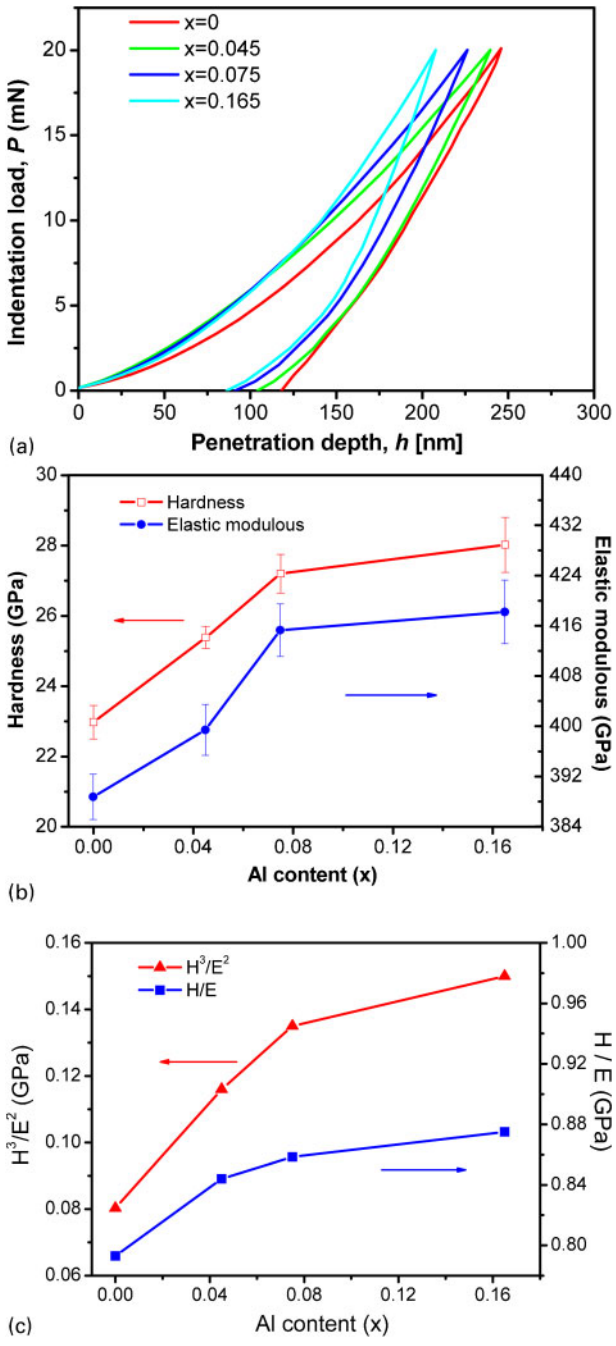

4 (a) Load-displacement curves of the $Mo(Si_{1-x}Al_x)_2$ coating under a maximum load of 20 mN; (b) The variation of the hardness and the elastic modulus with Al content in the coatings; (c) The variation of the ratio of H/E and H^3/E^2 with Al content in the coatings

of 3 mm. The nominal composition was Ti–6·04Al–4·03V–0·3Fe–0·1C–0·015H–0·05N–0·15O (wt-%). Before deposition, the Ti–6Al–4V substrates were polished using silicon carbide abrasive paper of 2400 grit and then ultrasonically cleaned in pure alcohol. Four kinds of nanocrystalline $Mo(Si_{1-x}Al_x)_2$ (x=0, 0·045, 0·075 and 0·165) coatings were deposited on Ti–6Al–4V alloy substrates using four targets with different stoichiometric ratios ($Mo_{25}Si_{75}$, $Mo_{25}Si_{70}Al_5$, $Mo_{25}Si_{65}Al_{10}$ and $Mo_{25}Si_{60}Al_{15}$) respectively. The reasons for such a difference in the composition of the targets and the as deposited coatings are that the composition of the as deposited coatings is related to not only the composition of targets materials but also the sputtering yields of the various elements in the target materials. Furthermore, the diffusion of different alloying elements at the interface between the as deposited coatings and substrate also affects the final composition of the coatings.

The phase compositions of the as deposited coatings were studied by XRD (D8ADVANCE with Cu K_α radiation) operated at 35 kV and 40 mA. X-ray data were collected using a 0·1° step scan with a count time of 1 s. The microstructures of the as deposited coatings were examined using SEM (Quanta200, FEI Company) incorporating an X-ray energy dispersive spectroscopy (EDS; EDAX Inc.) analyser attachment and field emission TEM (Philips CM200, Eindhoven, The Netherlands). The etching of the as deposited coatings was accomplished with the use of Kroll's reagent (10 mL HNO_3, 4 mL HF and 86 mL distilled water) for 20–30 s. Thin foil specimens for plan view TEM samples were prepared by cutting, grinding, dimpling and a final single jet electropolishing from the untreated side of the substrate at low temperature.

Nano-indentation tests were conducted on all the as deposited coatings using a nano-indentation tester equipped with a Berkovich diamond tip. This system, developed by CSEM Instruments, comprises two

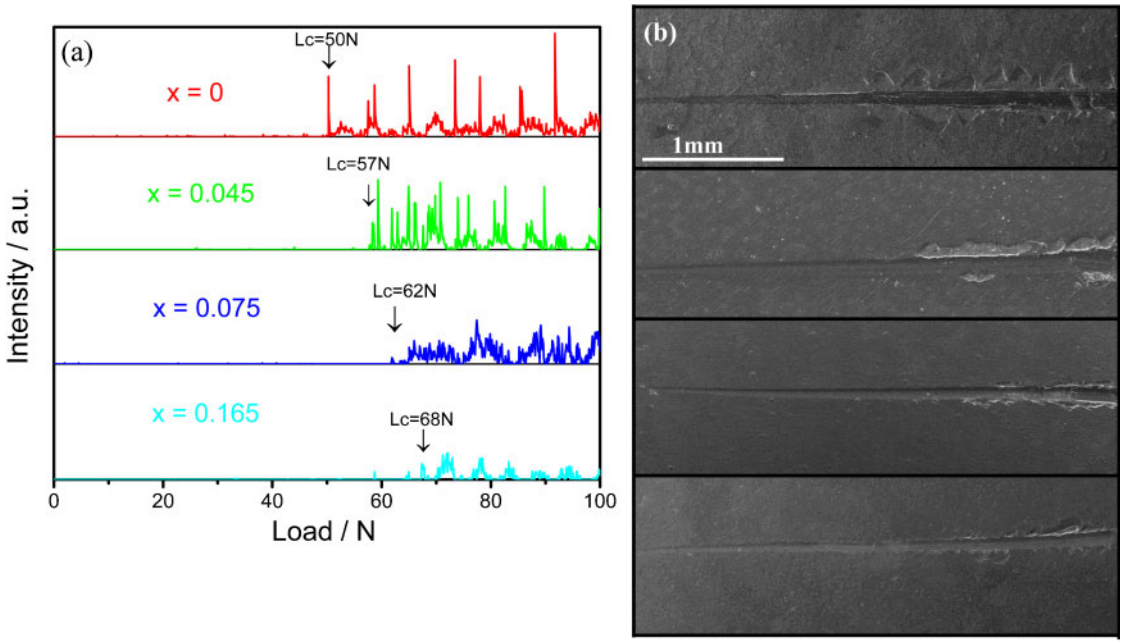

5 (a) Acoustic emission signal peaks vs. normal load curves of $Mo(Si_{1-x}Al_x)_2$ coating; (b) The corresponding SEM micrographs of the scratch tracks

distinct components: a measuring head for performing nano-indentation and an optical microscope for selecting a specific sample site before indentation and for checking the location of the imprint after indentation. The system has load and displacement resolutions of 10 mN and 1 nm respectively. Fused silica was used as a standard sample for the initial tip calibration. The indentation was performed by driving the indenter at a constant loading rate of 40 mN min^{-1} into the material surface with the maximum applied load of 20 mN. Hardness and the elastic modulus were evaluated using the Oliver–Pharr method[19] based on the load displacement data obtained during the indentation tests. Each hardness and elastic modulus data were derived from the load displacement curves of at least five indentations to ensure repeatability of the experimental data. Adhesion strength of the as deposited coatings was measured by a commercial scratch tester (WS-97), equipped with an acoustic emission (AE) detector. The scratch tests were performed by drawing a 200 μm radius Rockwell C diamond indenter across the coating surfaces under a normal load increasing linearly from 0 to 100 N. The loading rate was set at 20 N min^{-1}, and the scratch speed was 1 mm min^{-1}. An AE sensor was attached near the diamond indenter tip to detect the acoustic signals emitted from the coating failure. The minimum load at which a sudden increase in the intensity of the acoustic signals occurs is defined as the critical load L_c, which represents the coating adhesion strength.

The friction and wear tests were conducted using an HT-500 ball-on-disc type tribometer under dry conditions at room temperature in air with a relative humidity of 40–45%. In the present work, the balls, each 3 mm in diameter, were made of ZrO_2 with a hardness of 1300 HV and the lower disc samples ($10 \times 10 \times 3$ mm) were machined from both the uncoated substrate and the coated alloys. During the wear test, the ceramic ball was slid on the specimen surface describing a circle with a diameter of 6 mm at a sliding velocity of 0·176 m s^{-1} under the applied normal loads of 2·8 and 4·3 N respectively. The friction coefficient was continuously recorded using a Dell PC connected to the ball-on-disc test rig. The duration time of each test was 30 min, which corresponded to a sliding distance of 316·8 m. The profiles of the worn surfaces were measured using a MicroXAM non-contact optical profilometer (ADE Phase-Shift, USA), and the worn volume loss was evaluated by calculating the cross-sectional areas of worn tracks developed on the surface of the samples. The morphologies and phase compositions of worn surfaces were analysed by SEM (Quanta200, FEI Company) and XPS. The XPS measurements were carried out by Kratos AXIS Ultra ESCA System using Al K_α (1486·71 eV, pass energy of 20 eV).

Results

Microstructures and phase analysis

Figure 1 shows the XRD patterns for the as deposited $Mo(Si_{1-x}Al_x)_2$ (x=0, 0·045, 0·075 and 0·165) coatings. It can be seen that for all the as deposited coatings, only Bragg peaks corresponding to hexagonal C40 $MoSi_2$ are identified and the strong intensity of C40 $MoSi_2$ (111) peak at 41·36° indicates the as deposited coatings with a preferred (111) orientation. Furthermore, with increasing Al content, there is shift of the peaks of the C40 $Mo(Si_{1-x}Al_x)_2$ towards a lower 2θ values compared with the powder diffraction file data. The results show that the substitution of Al for Si leads to a lattice expansion due to the larger atomic radius of Al compared to Si. Note that although C40–$MoSi_2$ is a metastable phase with respect to $C11_b$ $MoSi_2$ at ambient temperature, this metastable phase can be formed under non-equilibrium conditions, such as thin film deposition.[20] In our case, the growth of coatings by glow discharge deposition is analogous to other thin film deposition processes (e.g. physical vapour deposition). Under such conditions, the mechanism of phase formation in the coatings is governed by the nucleation model, suggesting that the

phase with either the fastest nucleation rate or the smaller nucleation barrier is most likely formed. Since C40–$MoSi_2$ (1·5 eV) has a lower activation energy for nucleation than $C11_b$ $MoSi_2$ (7·8 eV), the formation of C40–$MoSi_2$ is before that of $C11_b$ $MoSi_2$ during glow discharge deposition.[21] Figure 2 shows typical cross-section SEM images of the four kinds of as deposited $Mo(Si_{1-x}Al_x)_2$ coatings formed on Ti–6Al–4V alloy. Clearly, the as deposited coatings have dense microstructure, free of any visible microcracks or pores, and are securely anchored to the substrate. Through XRD and EDS analysis, the microstructure of the as deposited coatings is actually classified into two uniform layers, namely, a $Mo(Si_{1-x}Al_x)_2$ layer and a Mo diffusion layer. The Mo diffusion layer can be further divided into β phase layer and α''/α' phase layer from outside to inside, as described elsewhere.[22] It is evident from Fig. 2 that an increase in Al content has negligible impact on the thickness of a $Mo(Si_{1-x}Al_x)_2$ layer, but significantly increases the thickness of the Mo diffusion layer, due to the fact that the Al addition imparts more metallic character to the bonding in the molybdenum disilicide, leading to a reduction in the diffusional resistance of Mo inward into the substrate.[15] A typical plan view bright field TEM image and high resolution TEM image taken from the outermost layer of the as deposited $Mo(Si_{0·955}Al_{0·045})_2$ coating are shown in Fig. 3. It is clearly seen that the as deposited $Mo(Si_{0·955}Al_{0·045})_2$ coating shows a uniform distribution of grain size with an average at $\sim$5 nm. The strong diffracted intensity of the (111) ring provides further evidence that the as deposited $Mo(Si_{0·955}Al_{0·045})_2$ coating exhibits a strong (111) texture. The spacings of the lattice fringes of the crystallites marked by circles can be calculated as 2·18 Å, which corresponds to the interplanar distance for the (111) lattice plane of the hexagonal C40 $MoSi_2$.

Nano-indentation and scratch tests

Figure 4*a* illustrates typical load–displacement (*p*–*h*) curves for the as deposited $Mo(Si_{1-x}Al_x)_2$ coatings indented with a maximum load of 20 mN. The maximum depth of the diamond indenter penetration into the coatings and residual depth decrease with increasing *x* values. It is to be noted here that for thin hard coatings on ductile substrates, if the maximum indentation depth is smaller than 10% of the as deposited coatings thickness, the contribution to measured mechanical properties from its substrate is negligible. Therefore, the results of indentation measurements reported here should accurately reflect the mechanical behaviour of as deposited coatings. Figure 4*b* shows the hardness and the elastic modulus calculated using Oliver–Pharr method based on the load displacement data obtained from the as deposited $Mo(Si_{1-x}Al_x)_2$ coatings. The results show that the hardness and elastic modulus of the as deposited $Mo(Si_{1-x}Al_x)_2$ coatings increase with increasing Al addition. Although hardness has long been regarded as a primary material property to evaluate the wear resistance of materials based on classical theories of wear, many researchers have proposed that the elastic strain to failure (H/E) and plastic deformation resistance factor (H^3/E^2) are more suitable parameters for predicting wear resistance than hardness alone.[23,24] Figure 4*c* shows the variation of the ratio of H/E and H^3/E^2 with Al content in the coatings. It can be seen that the ratio of H/E and H^3/E^2 for the as deposited $Mo(Si_{1-x}Al_x)_2$ coatings

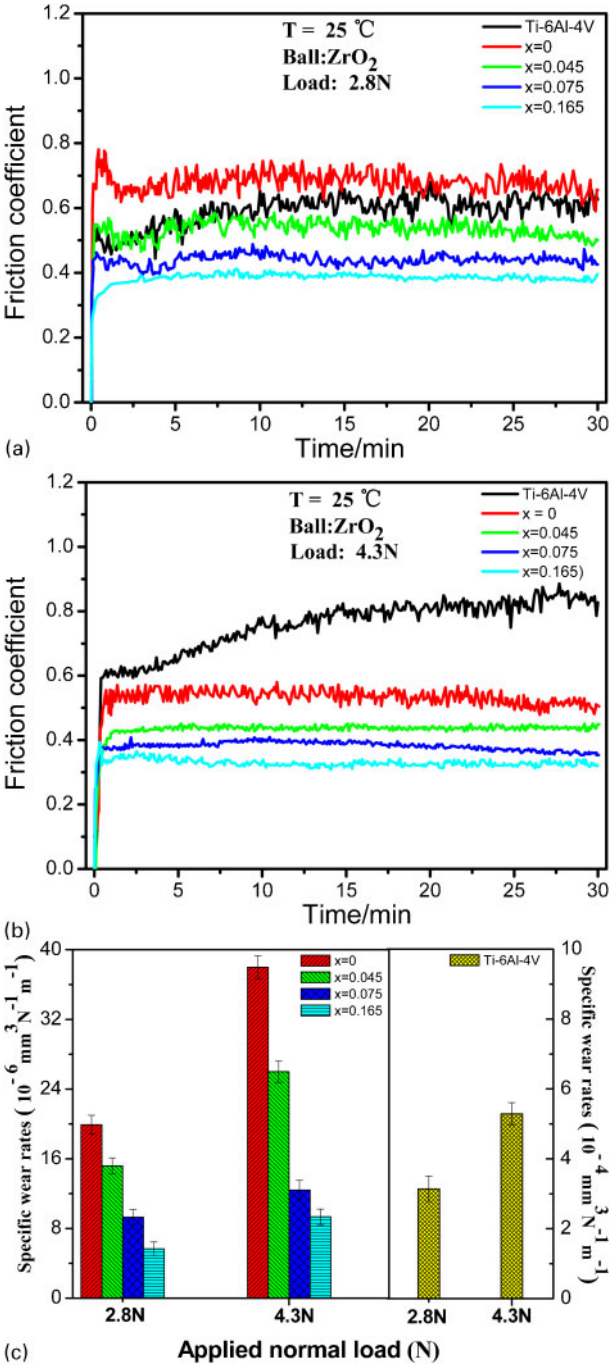

6 Coefficient of friction vs. sliding times and specific wear rates for the four as-deposited $Mo(Si_{1-x}Al_x)_2$ coatings and the uncoated Ti-6A1-4V alloy under two applied normal loads. (a) Friction coefficient under the load of 2·8N; (b) Friction coefficient under the load of 4·3N. (c)The specific wear rates for the four as-deposited $Mo(Si_{1-x}Al_x)_2$ coatings and the uncoated Ti-6A1-4V alloy

also increases monotonically with increasing Al content in the coatings, indicative of a potential increase in wear resistance of $Mo(Si_{1-x}Al_x)_2$ coatings by the addition of Al.

The scratch resistance is a good indicator of not only adhesion strength between the coating and the substrate but also the load bearing capacity, fracture toughness and abradability of a coating.[25–27] A commercial scratch tester was used to estimate the adhesion strength and

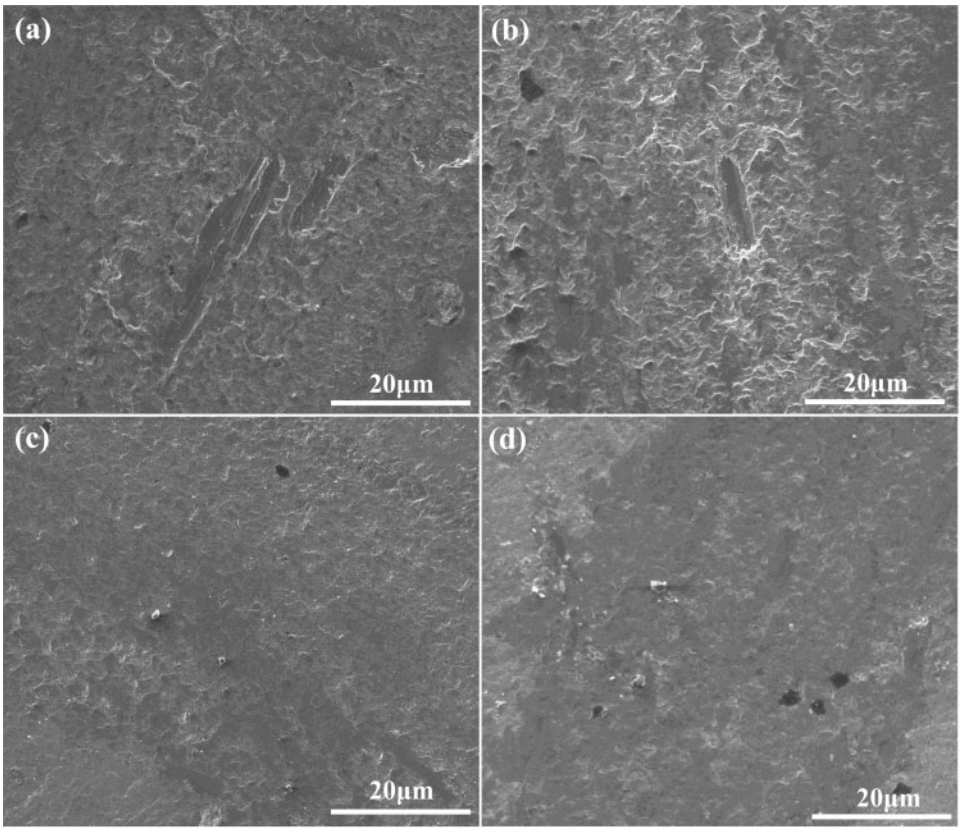

7 The SEM images of the worn surfaces of the as-deposited $Mo(Si_{1-x}Al_x)_2$ coatings sliding against ZrO_2 ceramic balls under the normal loads of 4·3N. (a) $MoSi_2$ coating; (b) $Mo(Si_{0.955}Al_{0.045})_2$ coating; (c) $Mo(Si_{0.925}Al_{0.075})_2$ coating; (d) $Mo(Si_{0.835}Al_{0.165})_2$ coating

damage responses of the as deposited coatings on the substrates. The AE curves of the as deposited $Mo(Si_{1-x}Al_x)_2$ coatings are plotted as a function of the normal load in Fig. 5*a*, and the corresponding SEM images of scratch tracks are displayed in Fig. 5*b*. All curves show an abrupt increase in AE signals when the scratching load reaches a critical load. As shown in Fig. 5*b*, the width of scratched tracks increases with the increase in the applied scratch loads. The scratch tracks show smooth morphologies without detectable delamination or microcracks, at the scratch loads below the critical loads, and subsequently, microcracks perpendicular to the scratch direction accompanied by chipping of the coatings along the sides of the scratch track are observed when the scratching loads exceed the critical loads that the coatings could support. It is evident that the critical loads increase with the content of Al in the coatings. The results can be explained from the fact that a marked increase in the thickness of the Mo diffusion layer by Al addition is favourable for lowering stress concentrations at the interface when the coatings are subjected to external loads.

Friction and wear

The variation of friction coefficient as a function of sliding time under two applied normal loads for the four as deposited $Mo(Si_{1-x}Al_x)_2$ coatings and the uncoated Ti–6A1–4V sliding against ZrO_2 ceramic balls is plotted in Fig. 6*a* and *b*. All measured friction curves presents a strong similarity in shape and are characterised by two distinguishable stages. At the first stage, the friction coefficient increases rapidly, followed by a second stage where the friction coefficient reaches a steady state value. For the $MoSi_2$ coating, the steady state friction coefficient is higher than that of the uncoated substrate at a normal load of 2·8 N, while an opposite tendency is observed at the higher normal load of 4·3 N. On the contrary, the steady state friction coefficients for the $Mo(Si_{1-x}Al_x)_2$ (x=0·045, 0·075 and 0·165) coatings are lower than those for the uncoated Ti–6A1–4V alloy under each tested load. Figure 6*c* shows the variation of specific wear rates as a function of the applied load for the as deposited coatings and the uncoated Ti–6A1–4V at a fixed sliding time. The specific wear rates increase with an increase in the load for all of the tested samples. Under the same tested load, the specific wear rates of the as deposited coatings decrease with increasing Al content and are dramatically reduced by >1–2 orders of magnitude over the uncoated Ti–6A1–4V, indicating that the as deposited $Mo(Si_{1-x}Al_x)_2$ coatings may effectively enhance the wear resistance of Ti–6A1–4V alloy. The change tendency of specific wear rates is also in accordance with that of the ratios of H^3/E^2 and H/E for the as deposited $Mo(Si_{1-x}Al_x)_2$ coatings. Figure 7 shows the SEM images of the worn surfaces of the as deposited $Mo(Si_{1-x}Al_x)_2$ coating sliding against ZrO_2 ceramic ball under the normal loads of 4·3 N. As shown in Fig. 7*a* and *b*, the worn surfaces of the $Mo(Si_{1-x}Al_x)_2$ (x=0 and 0·045) coatings appear to be very loose and rough, consisting of numerous large craters resulting from brittle detachment, together with parallel grooves formed by plowing action. In contrast, the $Mo(Si_{1-x}Al_x)_2$ (x=0·075 and 0·165) coatings show rather dense and smooth worn surfaces, showing no

sign of delamination or wear grooves, as shown in Fig. 7*c* and *d*. To determine whether or not the relevant tribochemical reactions take place during the dry sliding wear process of the coatings, XPS analysis was performed on the $Mo(Si_{1-x}Al_x)_2$ (x=0 and 0·075) coatings, as shown in Fig. 8. As shown in Fig. 8*a*, the Mo 3d spectra consists of doublet peaks Mo $3d_{5/2}$ and Mo $3d_{3/2}$ at 233 and 236·1 eV, which are designated as MoO_3. As shown in Fig. 8*b*, the Si 2p spectra show a single peak at a binding energy of 103 eV, which is typical of Si in the form of SiO_2. As expected, Al 2p peaks are detectable from the worn surface of the $Mo(Si_{0·925}Al_{0·075})_2$ coating. As shown in Fig. 8*c*, the Al 2p spectra show one component with a binding energy of 75·0 eV corresponding to Al_2O_3.

Discussion

Experimental results above indicate that the addition of Al has an important impact on mechanical properties of the coatings, adhesion strength between the coatings and the substrate, and the behaviour of the tribochemical layer, and those factors play key roles in determining the wear process of the coatings. For C40 $MoSi_2$, only basal slip along $\langle 11\bar{2}0\rangle$ on (0001) is operative and no other slip systems are observed in the temperature range from room temperature to 1500°C. Inui *et al.*[28] suggested that for C40 structured $MoSi_2$, basal slip appears to occur through a synchroshear mechanism, in which a sequence of shears occurs synchronously on two adjacent (0001) planes, and these are involved in a C40→$C11_b$ phase transformation. Therefore, alloying C40 $MoSi_2$ with Al that forms a C40 structured disilicide would increase the energy difference between C40 and $C11_b$ structures, and thus, the Peierls stress changes accordingly, resulting in solid solution hardening. Harada *et al.*[29] also found that Al additions in $Mo(Si_{1-x}Al_x)_2$ up to about x=0·15 resulted in the formation of C40 structured $MoSi_2$, and its hardness increases gradually with Al content. The abovementioned theoretical analysis is in complete accord with the experimental data determined by nano-indentation. Furthermore, in terms of the parameters of H/E and H^3/E^2 and results of scratch tests, alloying C40 $MoSi_2$ with Al can not only enhance the resistance to plastic deformation but also improve the load bearing capacity of the as deposited coatings. During the wear process, the friction force is partly attributed to the force needed in the plastic deformation of the $Mo(Si_{1-x}Al_x)_2$ coatings. With a higher Al content, the depth that the hard asperities of counterpart ZrO_2 ceramic ball penetrate the $Mo(Si_{1-x}Al_x)_2$ coatings is smaller, and accordingly, the force required for the plastic deformation is smaller. Therefore, the friction coefficients of the $Mo(Si_{1-x}Al_x)_2$ coatings decrease with a further increase in the amount of Al addition.

Under conditions of dry sliding wear, due to the combined effect of tribothermal and tribomechanical, the $Mo(Si_{1-x}Al_x)_2$ nanocrystalline coatings, with a higher surface activity and more grain boundaries, easily react with oxygen present in the air, and hence, the formation of tribochemical layers is produced on the worn surface, as confirmed by XPS analyses. Based on the observations of the worn surface topography, the tribochemical layers formed on the $Mo(Si_{1-x}Al_x)_2$ (x=0 and 0·045) coatings show poorly protective effectiveness and are readily plastic removal and detached from the worn surfaces. In contrast, the continuous and dense tribochemical layers are well adhered to the $Mo(Si_{1-x}Al_x)_2$ (x=0·075 and 0·165) coatings and provide the solid lubrication action, weakening the scratching effect and reducing the wear rates of the coatings. Moreover, no significant changes in the grain sizes and hardness of Ti–6Al–4V alloy were observed before and after surface treatment of double cathode glow discharge, suggesting that the nanocrystalline $Mo(Si_{1-x}Al_x)_2$ coatings prepared by double cathode glow discharge technique is expected to be a feasible method for improving the wear resistance of Ti alloys.

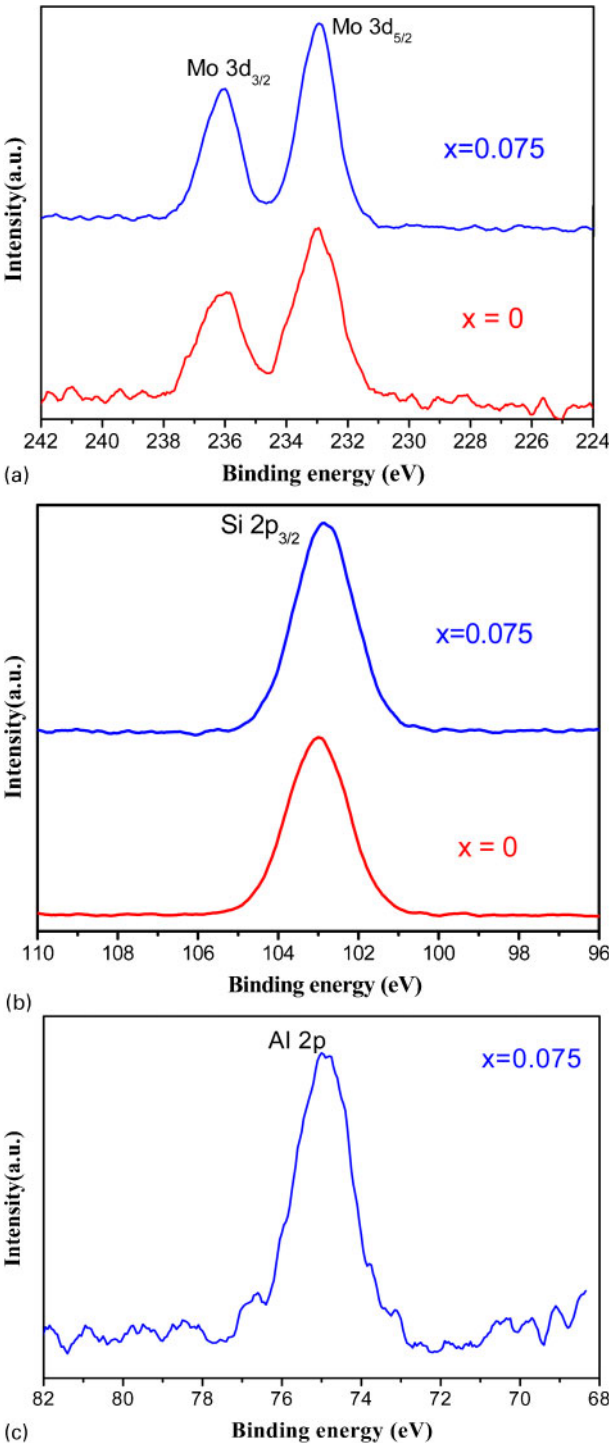

8 XPS analysis on the worn surfaces of $Mo(Si_{1-x}Al_x)_2$ (x=0 and 0·075) coatings (a) Mo 3d spectra; (b) Si 2p spectra; (c) Al 2p spectra

Conclusions

In summary, four kinds of C40 $Mo(Si_{1-x}Al_x)_2$ nanocrystalline coatings with varying Al contents were prepared on Ti–6Al–4V alloy substrate by a double cathode glow discharge apparatus. The resultant coatings with the average grain size of ~5 nm show a strong (111) preferred orientation. The hardness elastic strain to failure (H/E) and plastic deformation resistance (H^3/E^2) of the $Mo(Si_{1-x}Al_x)_2$ coatings increase with increasing Al addition. Under the same tested load, the specific wear rates of the $Mo(Si_{1-x}Al_x)_2$ coatings decrease with increasing Al content and are dramatically reduced by more than 1–2 orders of magnitude compared with the uncoated Ti–6A1–4V. The results show that both the mechanical properties and the formation of the tribochemical layers on the worn surfaces play vital roles in determining the wear resistance of the $Mo(Si_{1-x}Al_x)_2$ coatings.

Acknowledgement

The authors acknowledge the financial support of the National Natural Science Foundation of China under grant no. 51175245.

References

1. S. Fouvry, C. Paulin and S. Deyber: *Tribol. Int.*, 2009, **42**, 461–474.
2. D. G. Bansal, O. L. Eryilmaz and P. J. Blau: *Wear*, 2011, **271**, 2006–2015.
3. H. Schmidt, A. Schminke, M. Schmiedgen and B. Baretzky: *Acta Mater.*, 2001, **49**, 487–495.
4. K. T. Rie, T. Stucky, R. A. Silva and E. Leitao: *Surf. Coat. Technol.*, 1995, **74–75**, 973–980.
5. M. Ueda, M. M. Silva, C. Otani, H. Reuther, M. Yatsuzuka and C. M. Lepienski: *Surf. Coat. Technol.*, 2003, **169–170**, 408–410.
6. H. M. Wang, F. Cao, L. X. Cai, H. B. Tang, R. L. Yu and L. Y. Zhang: *Acta Mater.*, 2003, **51**, 6319–6327.
7. J. A. Hawk and D. E. Alman: *Scr. Metall. Mater.*, 1995, **32**, 725–730.
8. H. J. Chen, W. M. Rainforth and W. E. Lee: *Scr. Mater.*, 2000, **42**, 555–560.
9. A. Rico, J. Rodriguez, E. Otero, P. Zeng and W. M. Rainforth: *Wear*, 2009, **267**, 1191–1197.
10. T. C. Lu, A. G. Evans, R. J. Hecht and R. Mehrabian: *Acta Metall. Mater.*, 1991, **39**, 1853–1862.
11. B. K. Yen, T. Aizawa and J. Kihara: *J. Am. Ceram. Soc.*, 1996, **79**, 2221–2225.
12. H. Inui, K. Ishikawa and M. Yamaguchi: *Intermetallics*, 2000, **8**, 1131–1145.
13. U. V. Waghmare, E. Kaxiras, V. V. Bulatov and M. S. Duesbery: *Modell. Simul. Mater. Sci. Eng.*, 1998, **6**, 493–506.
14. U. V. Waghmare, V. Bulatov, E. Kaxiras and M. S. Duesbery: *Mater. Sci. Eng. A*, 1999, **A261**, 147–157.
15. D. M. Shah, D. Berczick and D. L. Anton: *Mater. Sci. Eng. A*, 1992, **A155**, 45–57.
16. T. Dasgupta and A. M. Umarji: *Intermetallics*, 2007, **15**, 128–132.
17. Y. J. Qiao, H. X. Zhang, C. Q. Hong and X. H. Zhang: *J. Phys. D*, 2009, **42D**, 105413–105424.
18. J. Xu, Z. Xu, J. Tao, Z. L. Liu, Z. Y. Chen and W. H. Zhu: *Scr. Mater.*, 2007, **57**, 587–590.
19. W. C. Oliver and G. M. Pharr, *J. Mater. Res.*, 1992, **7**, 1564–1583.
20. P. S. Frankwicz and J. H. Perepezko: *Mater. Sci. Eng. A*, 1998, **A246**, 199–206.
21. E. Chi, J. Shim, J. Kwak and H. Balk: *J. Mater. Sci.*, 1996, **31**, 3567–3572.
22. J. Xu, Y. Wang and S. Y. Jiang: *Nanoscale*, 2010, **2**, 394–398.
23. A. Leyland and A. Matthews: *Surf. Coat. Technol.*, 2004, **317**, 177–178.
24. M. E. Roy, L. A. Whiteside, J. Xu and B. J. Katerberg: *Acta Biomater.* 2010, **6**, 1619–1624.
25. Z. Chen, Y. L. W. Linda, E. Chwa and O. Tham: *Mater. Sci. Eng. A*, 2008, **A493**, 292–298.
26. X. Ma and A. Matthews: *Surf. Coat. Technol.*, 2007, **202**, 1214–1220.
27. Z. X. Zhang, H. Dong and T. Bell: *Surf. Coat. Technol.*, 2006, **200**, 5237–5244.
28. H. Inui, M. Moriwaki, K. Ito and M. Yamaguchi: *Philos. Mag. A*, 1998, **77A**, 375–394.
29. Y. Harada, Y. Murata and M. Morinaga: *Intermetallics*, 1998, **6**, 529–535.